High volumetric capacity three-dimensionally sphere-caged secondary battery anodes

Jinyun Liu,[†,‡] Xi Chen,[ζ] Jinwoo Kim,[‡] Qiye Zheng,[‡] Hailong Ning,[Δ] Pengcheng Sun,[‡] Xingjiu Huang,[†] Jinhuai Liu,[†] Junjie Niu,[ζ] and Paul V. Braun[,‡]*

[†] Nanomaterials and Environmental Detection Laboratory, Institute of Intelligent Machines, Chinese Academy of Sciences, Hefei, Anhui 230031, China.

[‡] Department of Materials Science and Engineering, Department of Chemistry, Frederick Seitz Materials Research Laboratory, and Beckman Institute for Advanced Science and Technology, University of Illinois at Urbana-Champaign, Urbana, Illinois 61801, USA.

[Δ]Xerion Advanced Battery Corp., Champaign, Illinois 61820, USA.

[ζ] Department of Materials Science and Engineering, University of Wisconsin-Milwaukee, Milwaukee, Wisconsin 53201, USA.

* Correspondence should be addressed to P.V.B. (E-mail: pbraun@illinois.edu).

ABSTRACT:

High volumetric energy density secondary batteries are important for many applications, which has led to considerable efforts to replace the low volumetric capacity graphite-based anode common to most Li-ion batteries with a higher energy density anode. Because most high capacity anode materials expand significantly during charging, such anodes must contain sufficient porosity in the discharged state to enable the expansion, yet not excess porosity, which lowers the overall energy density. Here, we present a high volumetric capacity anode consisting of a three-dimensional (3D) nanocomposite formed in only a few steps which includes both a 3D structured Sn scaffold and a hollow Sn sphere within each cavity where all the free Sn surfaces are coated with carbon. The anode exhibits a high volumetric capacity of ~1700 mAh cm^{-3} over 200 cycles at 0.5C, and a capacity greater than 1200 mAh cm^{-3} at 10C. Importantly, the anode can even be formed into a commercially relevant ~100 μm-thick form. When assembled into a full cell the anode shows a good compatibility with a commercial $LiMn_2O_4$ cathode. *In-situ* TEM observations confirm the electrode design accommodates the necessary volume expansion during lithiation.

KEYWORDS: Li-ion battery; volumetric capacity; *in-situ* TEM; mesostructure

Secondary batteries have received broad attention due to their applications in fields ranging from portable electronic devices to electric vehicles.[1–5] For many applications, where space is often limited, the volumetric energy density is particularly significant, which has led to interest in anode materials other than carbon. Graphite-based anodes have a rather low volumetric capacity (theoretical 818 mAh cm^{-3}, and practical ~550 mAh cm^{-3}),[6,7] relative to a material such as tin, which on an alloying/de-alloying mechanism basis, possesses a theoretical volumetric capacity of 2017 mAh cm^{-3} ($Li_{4.4}Sn$ lithiated volume basis).[8] In addition, the tin lithiation potential is slightly higher than graphite (~0.5 V *vs.* Li/Li^+),[9,10] reducing the potential risk of Li-plating during charging.[11] However, the large volume expansion (~260%) and the resulting cracking and pulverization of tin during charge-discharge cycling commonly results in a rapid capacity fade.[12,13]

To accommodate the volume change of high capacity materials such as tin during cycling, both active material nanostructuring and electrode mesostructuring have been considered. Previous reports from us[14–17] and others[18–21] on three-dimensional (3D) porous secondary battery electrodes show some performance advantages through electrode mesostructuring, however, the active material loading of the electrodes are generally low, resulting in a lower than desired full electrode-basis volumetric capacity. In the literature, it has been shown how encapsulating active materials inside shells may provide a path to improving the volumetric capacity of high-capacity materials that undergo significant volume changes.[22,23]

Here, we present a high volumetric capacity anode consisting of a 3D Sn scaffold containing a Sn hollow sphere within each cavity where all the Sn surfaces are coated with carbon. Relative to a simple Sn foam structure, the addition of the Sn hollow spheres increases the active material loading, while the 3D structure allows the active material to change in volume during cycling without a change in the overall electrode dimensions. In a single infilling process, assuming an ideal

opal template, the theoretical maximum filing fraction before pinch-off is about 22%,[24] and from our experience experimentally is often less, while via the two-layer approach presented here, the filling fraction is ~27% (higher infilling may be possible, but is not desirable, as it would result in closure of the pore network during lithiation-induced swelling of the active material). The carbon coating likely improves the stability of the solid electrolyte interphase (SEI) that forms during cycling. Figure 1 outlines the fabrication route. First, a SnO_2 scaffold was fabricated by a two-step procedure starting from a 3D polystyrene (PS) structure. A SiO_2 layer was coated onto the SnO_2, followed by hydrothermal growth of SnO_2 and SiO_2 removal, resulting in SnO_2 spheres caged within a SnO_2 foam. Finally, following a carbon-coating treatment, the SnO_2 was reduced to Sn metal, forming a 3D sphere-caged Sn/C composite anode which exhibits a volumetric capacity of ~1700 mAh cm^{-3} (over three times that of a carbon-based anode).

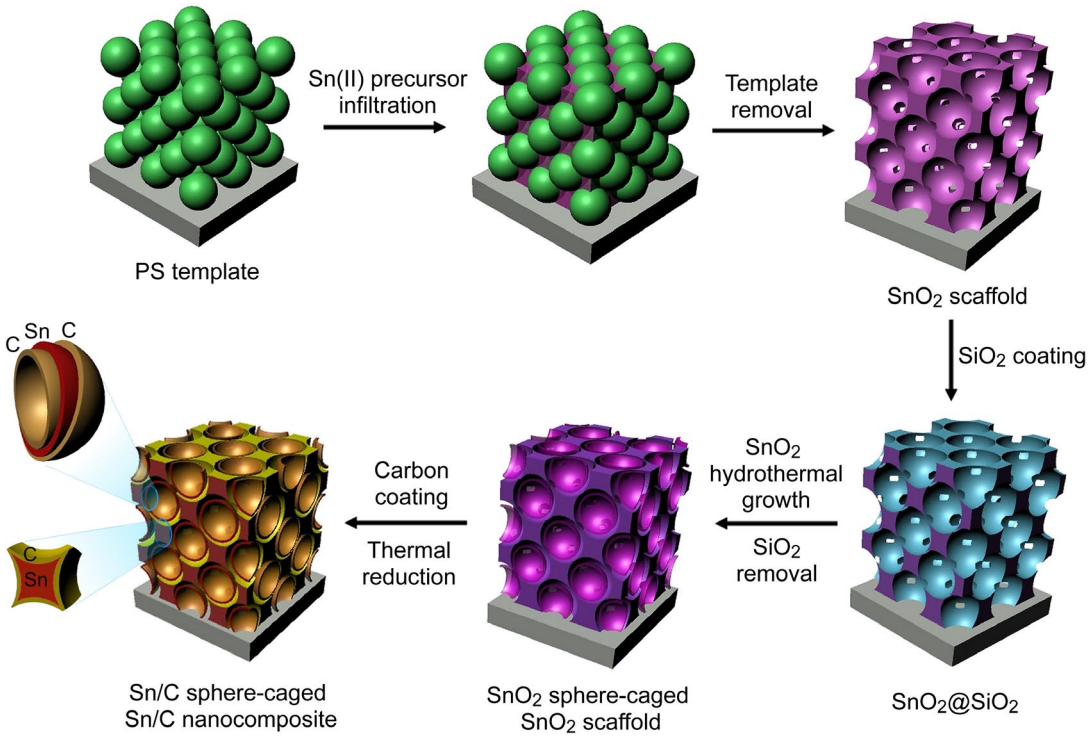

Figure 1. Schematic illustration of the three-dimensionally structured Sn-based anode fabrication process.

Morphologies during the fabrication process are shown in Figure 2. Use of a slightly sintered PS structure (Supporting Information Figure S1) results in a more interconnected pore network after template removal (Figure 2a) (interconnect window between adjacent cavities is about 170 nm). Low- and high-magnification scanning electron microscopy (SEM) images are shown in Supporting Information Figure S1c,d, and a 3D structure model is shown in Supporting Information Movie 1. The pores enable both the subsequent SiO_2 coating and the second SnO_2 hydrothermal growth to proceed throughout the electrode. Figure 2b shows the SnO_2 scaffold coated with a SiO_2 layer. Hydrothermal growth was conducted to form the encaged SnO_2 layer (Supporting Information Figure S1e,f). After SiO_2 removal, carbon coating and SnO_2 reduction, the 3D sphere-caged Sn/C nanocomposite anode shown in Figure 2c,d and Supporting Information Movie 2 was formed.

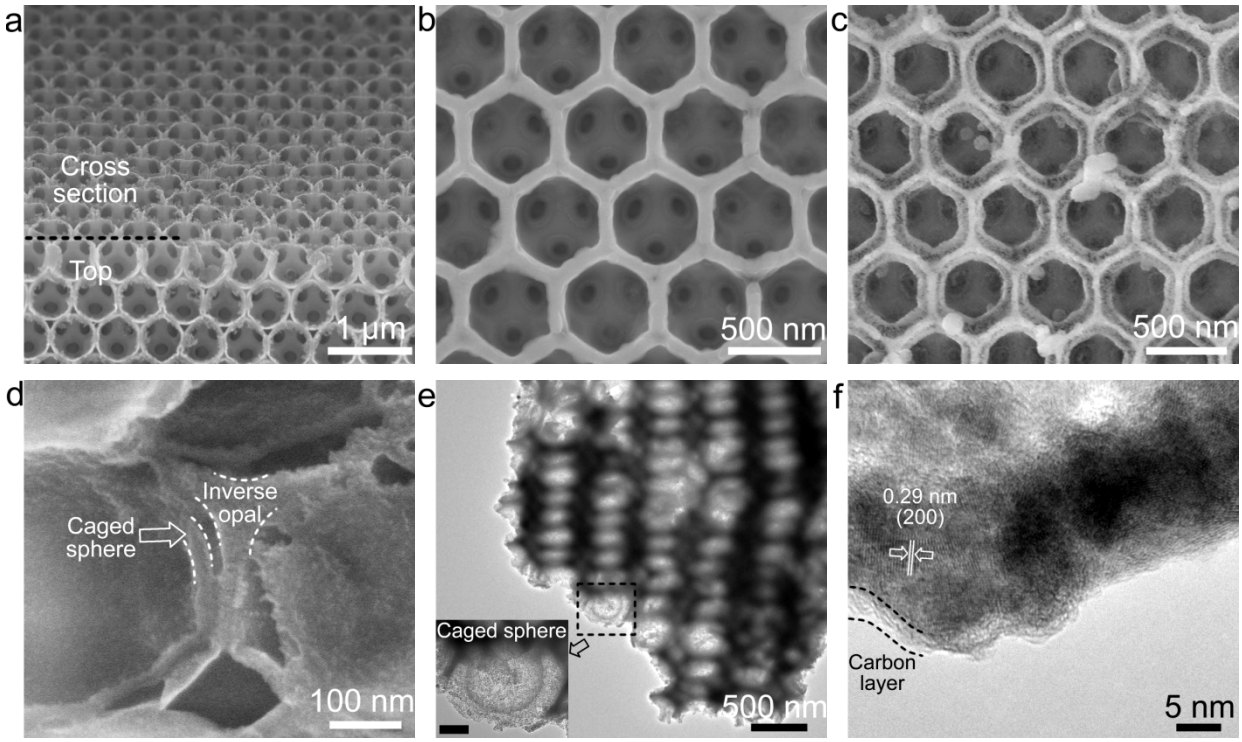

Figure 2. Morphology and structure during the anode fabrication. (a) SEM image of the SnO_2 scaffold after PS template removal. (b) SEM image of the SiO_2-coated SnO_2 inverse opal. (c) Top and (d) cross-sectional view SEM images of the Sn-based nanocomposite anode obtained by carbon coating followed by SnO_2 reduction. (e) TEM and (f) HRTEM images of the final nanocomposite anode. The scale bar in the inset of (e) is 100 nm.

In Figure 2c, a second layer of the Sn/C nanocomposite on the Sn/C scaffold can be observed. In the cross-sectional SEM (Figure 2d) and transmission electron microscopy (TEM) images (Figure 2e), a hollow sphere caged within each cavity of the scaffold, and a ~35 nm gap (volume previously occupied by the etched SiO_2) can be observed. Low-magnification cross-sectional SEM images (Supporting Information Figure S1g,h) confirm uniform caging of spheres throughout the scaffold. In the high-resolution TEM (HRTEM) image (Figure 2f), lattice fringes with spacing of 0.29 nm can be assigned to the (200) plane of Sn. A ~3 nm thick carbon layer is also observed. Raman spectroscopy (Supporting Information Figure S2) confirms the amorphous nature of the carbon, and thermogravimetric analysis (TGA) (Supporting Information Figure S3) indicates an overall electrode carbon content of about 5%. X-ray diffraction (Supporting Information Figure S4) confirms the Sn is tetragonal phase (Joint Committee on Powder Diffraction Standards card # 86–2264).

Figure 3a shows cyclic voltammetry (CV) curves for the first five cycles of the nanocomposite anode. In the first cathodic scan, the peak at about 0.8 V is ascribed to the SEI formation.[25] A series of reversible peaks between 0.7 and 0.3 V are attributed to the alloying of lithium-tin to form Li_xSn, while in the anodic scan the peaks between 0.5 and 0.8 V are assigned to the dealloying process,[26,27] as presented by $Sn + xLi^+ + xe^- \leftrightarrow Li_xSn$.[28] The peaks around 0.5 V in

the cathodic scan and 1.3 V in anodic scan which decay during cycling are likely electrochemical reactions between lithium and amorphous carbon.[29,30] The alloying and dealloying peaks overlap well starting with the second cycle, indicating stable and reversible lithiation-delithation.

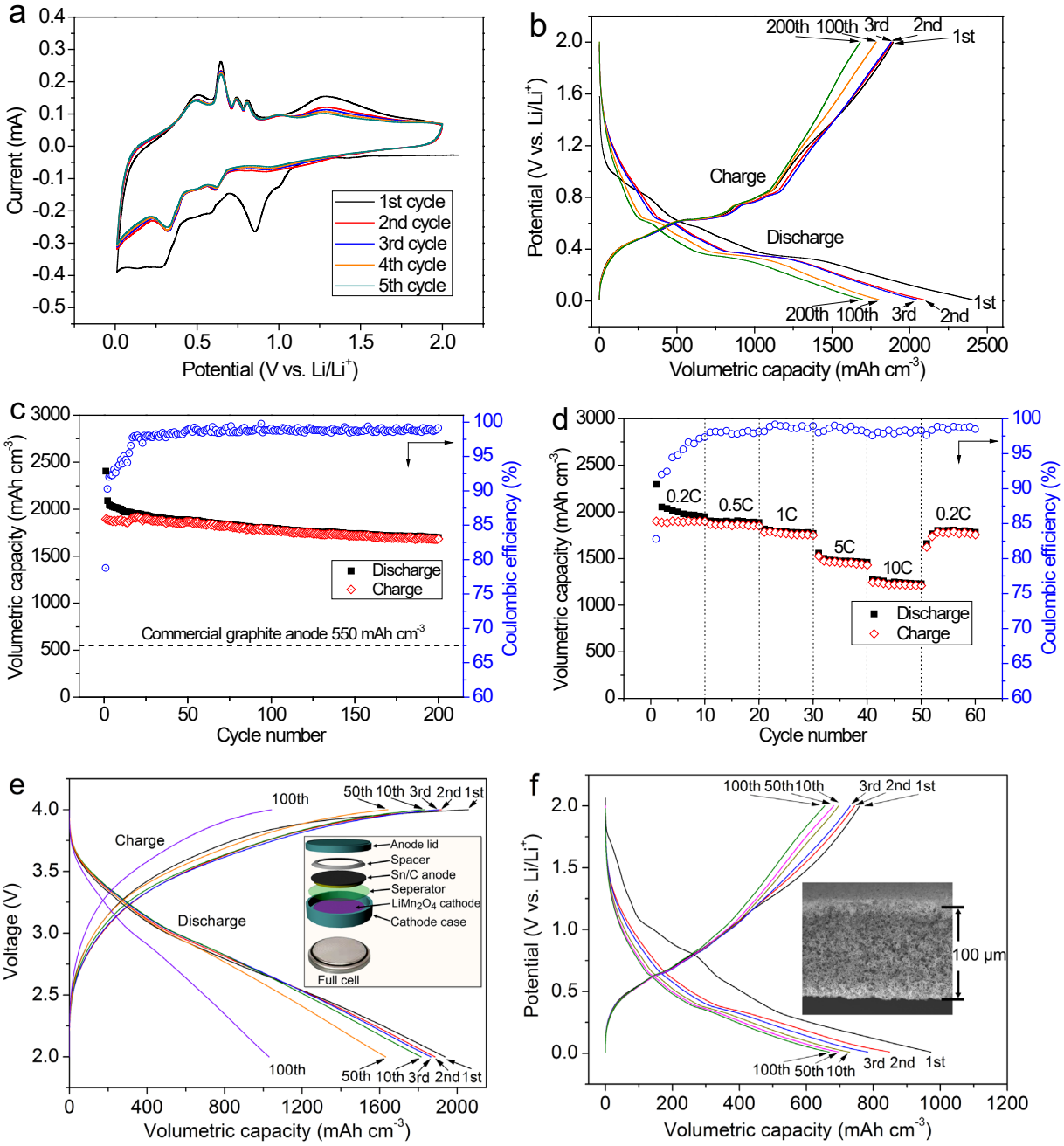

Figure 3. Electrochemical performance of the three dimensionally structured Sn-based anodes. (a) CV curves of the 3D Sn/C anodes over the potential range of 0 to 2 V *vs.* Li/Li^+ at a scan rate of 0.1

mV s^{-1}. (b) Galvanostatic charge-discharge curves of the sphere-caged Sn/C anodes at 0.5C from 0.01 to 2 V. (c) Cycling capacity and Coulombic efficiency over 200 cycles. All volumetric capacities are on a full electrode basis. (d) Capacity and Coulombic efficiency at varying C-rates. (e) Galvanostatic discharge-charge curves (at a rate of 0.5C based on the anode theoretical capacity) of a full cell fabricated using the sphere-caged Sn/C nanocomposite as anode *vs.* a commercial $LiMn_2O_4$ cathode. The inset in (e) illustrates the structure of the full cell. (f) The first, second, third, 10th, 50th, and 100th discharge-charge curves (at 1C) of a 100 μm-thick composite anode (cross-section illustrated by the inset) fabricated using a commercial Ni scaffold as the template.

The galvanostatic discharge-charge performance at 0.5C (1C corresponds to complete charge or discharge of theoretical capacity of tin in 1 h) for 200 cycles is shown in Figure 3b. The flat plateaus at around 0.7 to 0.3 V during the discharge (lithiation) are consistent with the CV profiles and previous reports on Sn-based anodes,[31,32] and can be ascribed to the alloying between tin and lithium to form Li_xSn. During charge (delithiation), the plateaus at ~0.4 to 0.8 V are assigned to the dealloying of Li_xSn. The electrode exhibits the first cycle discharge and charge volumetric capacities of ~2404 and 1894 mAh cm^{-3} on a full electrode basis, respectively, giving an first cycle Coulombic efficiency of 78.8% (Figure 3b,c) which increases to greater than 90% in the second cycle and to around 98% after ~15 cycles (the high first-cycle capacity is probably due to SEI formation). After 200 cycles, the discharge and charge capacities are about 1700 and 1682 mAh cm^{-3} (885 and 875 mAh g^{-1}), respectively, greater than the reported capacities of graphite-based anodes,[6,7] and many other anode systems.[33–35]

Figure 3d shows the rate performance of the 3D sphere-caged Sn/C anode (discharge-charge curves are shown in Figure S5). Both discharge and charge capacities decrease with increasing

C-rates. At 10C, the discharge and charge capacities are about 1229 and 1208 mAh cm^{-3}, respectively. When the C-rate returned to 0.2C, the discharge and charge capacities recovered to 1781 and 1754 mAh cm^{-3}. The good rate performance is probably due to the fact that all the Sn surfaces are coated with carbon, providing a conductive path for electron transfer, the mesoporous 3D structure provides a continuous network for liquid phase diffusion, and the Sn active material is thin. The properties of the fabricated anode were evaluated by electrochemical impedance spectroscopy (EIS) (Supporting Information Figure S6), which confirms a stable surface chemistry and consistent lithiation diffusion kinetics. All Nyquist plots collected at a series of discharge and charge stages consist of two semicircles in high and medium frequency regions and a straight line in the low frequency region. During discharge the medium frequency semicircle diameter decreases as discharge proceeds, indicating a decrease of charge transfer resistance as the anode lithiates; while during delithiation the charge transfer resistance increases (fitting data details shown in Supporting Information Table S1).

A full cell consisting of the Sn-based anode and a commercial $LiMn_2O_4$ cathode was constructed as illustrated by the inset in Figure 3e. The charge of the full cell corresponds to the lithiation of Sn/C anode; while discharge corresponds to delithiation. The $LiMn_2O_4$ cathode possesses an operating voltage of 3.9~4.1 V,[36,37] and the Sn-based anode exhibits lithiation and delithiation plateaus between 0.7~0.3 V and 0.4~0.8 V, respectively. Both the slight plateau at ~3.4 V and the sloping process starting from ~3.0 V during discharge in Figure 3e are ascribed to the Li-Sn alloying and the phase transformation of $LiMn_2O_4$ while the slight plateau starting from ~3.3 V during charging is attributed to dealloying.[38,39] From the second cycle onward, both charge and discharge become stable. After 100 cycles at 0.5C, the Sn/C anode retains a volumetric capacity of about 1020 mAh cm^{-3}, suggesting good compatibility with a commercial $LiMn_2O_4$

cathode at room temperature.

To evaluate the potential of the Sn/C nanocomposite anode for practical applications, where thick electrodes (*e.g.*, 100 μm) are generally required, ~100 μm-thick Sn/C anodes were fabricated using a commercial disordered mesostructured Ni scaffold as template. Here, it should be noted that to enhance the strength of the free-standing thick electrode, the Ni scaffold (Ni volume fraction 5%) and SiO_2 coating were retained within the electrode. The electrode fabrication process and the related material characterizations are shown in Supporting Information Figures S7 and S8. The discharge-charge curves of the 100 μm-thick Sn/C anode at a rate of 1C are shown in Figure 3f. Over 100 cycles, the anode retains a full electrode-basis volumetric capacity greater than 650 mAh cm^{-3}, and a higher active material loading may be possible through electrode structure optimizations.

Real time lithiation of the Sn/C nanocomposite anode was observed using a TEM attached with an *in-situ* holder in which a nanoscale battery system (half cell) consisting of Sn/C nanocomposite as the working electrode and a Li metal flake covered by a natural thin Li_2O solid electrolyte layer counter electrode (Figure 4a).[40]As shown in Figures 4b,c, an obvious volume expansion of the Sn/C composite particle occurred after contact with the Li flake as the lithium alloyed with the Sn. The dynamic structural evolution can be found in Supporting Information Movies 3 and 4. Selected area electron diffraction (SAED) patterns indicate a phase transformation from tetragonal Sn to a largely amorphous Sn-Li alloy which may also contain alloy phases such as Li_3Sn_5 during lithation (insets in Figure 4b). As seen in Figure 4c, the 3D structure is stable to lithiation. To confirm the overall electrode thickness does not change during cycling, the thickness of the thinner electrodes and the 100 μm-thick electrodes was measured via SEM after lithiation and delithiation (Supporting Information Figure S9), as well as by a micrometer before and after lithiation, and before and after

delithiation. No significant change in the overall electrode thickness during cycling is observed, probably because the engineered pores within the electrode accommodate the volume change.

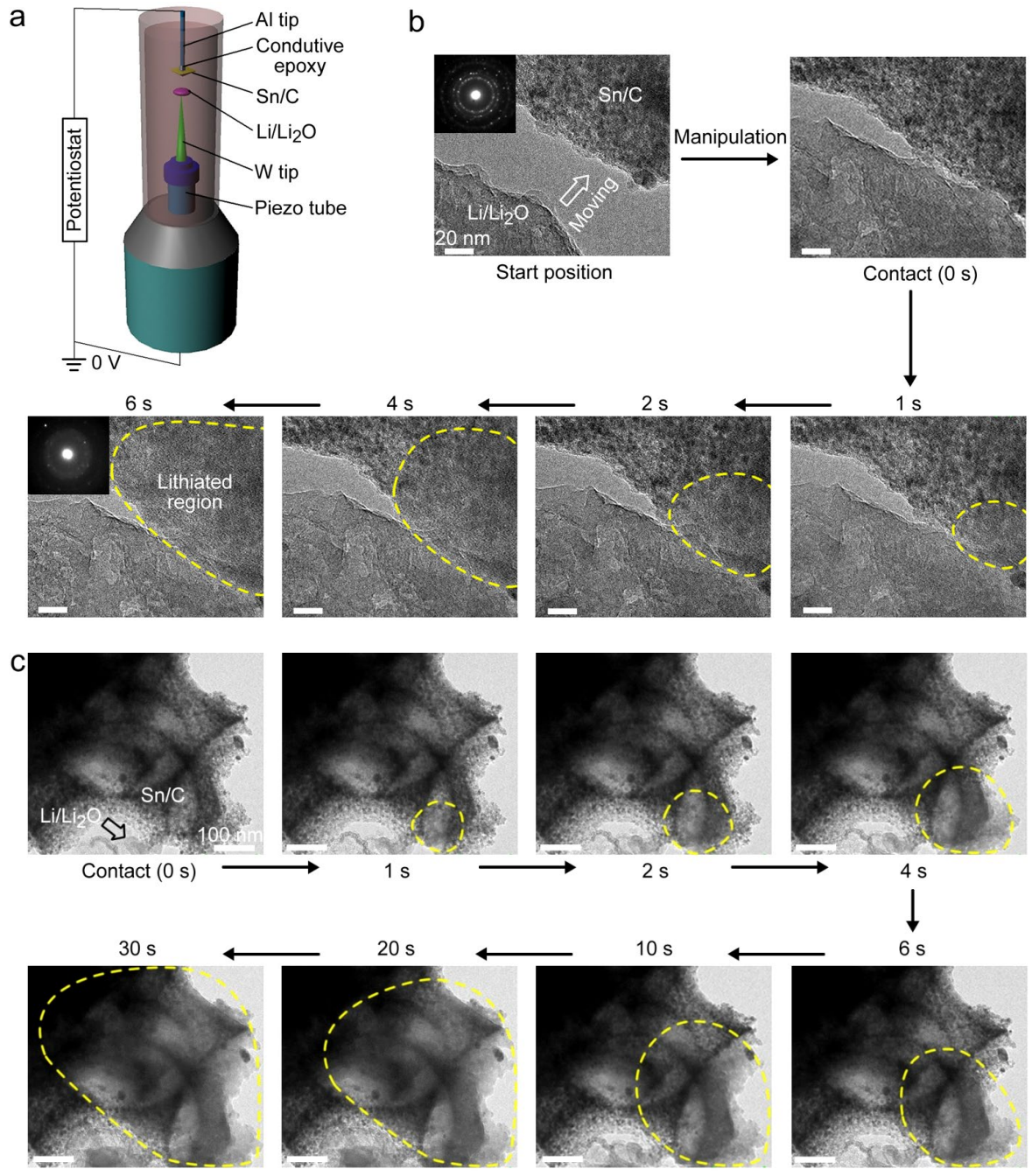

Figure 4. *In-situ* TEM observations. (a) Schematic illustration of the *in-situ* TEM of the Sn-based nanocomposite anode. (b) High, and (c) low-magnification TEM images during lithiation. The insets in (b) are SAED patterns.

In summary we present a high volumetric capacity anode consisting of a 3D Sn nanocomposite containing a Sn hollow sphere within each cavity where the free surfaces are coated with carbon. This anode exhibits a volumetric capacity of ~1700 mAh cm^{-3} over 200 cycles at 0.5C, and a good rate performance of about 1229 (discharge) and 1208 mAh cm^{-3} (charge) at 10C. Both a ~100 μm-thick Sn/C nanocomposite anode and a full cell consisting of the sphere-caged Sn/C anode *vs*. a commercial $LiMn_2O_4$ cathode exhibit high capacities. *In-situ* TEM observations confirm the anode structure has the ability to accommodate the volume expansion during lithiation, enabling a reversible high volumetric capacity. The high volumetric energy density of the anode presented here is expected to be important for a broad set of possible cathode chemistries.

Methods. *3D PS structure and SnO_2 scaffold fabrication. T*he PS structure were prepared on tungsten (W) substrates following our previous reports[14,16] with the modifications indicated here. The W foils (1.2 × 2 cm, 0.25 mm thick, ≥99.9% trace metals basis, Sigma-Aldrich Corp.) were cleaned by sonication in acetone and followed by Millipore water (18.2 MΩ cm resistivity) for 30 min each. Then PS colloid spheres (600 nm diameter, Molecular Probes) were dispersed in Millipore water, forming a 0.2 wt% suspension. After drying with blown N_2 gas, the W substrates were placed vertically into vials containing the PS suspension (about 1.5 cm depth; the final structure is about 1 cm long) at 55 °C. To enhance the bonding between PS spheres, the fabricated PS structures were sintered at 95 °C for 3 h. To fabricate the SnO_2 scaffolds, a Sn(II) precursor solution was prepared by mixing 0.2 g $SnCl_2{\cdot}2H_2O$ (Sigma-Aldrich Corp.), 10 mL ethanol, and a 0.1 M HCl solution (0.2 mL) under stirring for 2 h. The prepared precursor solution was then

statically aged for 48 h at room temperature before further usage. The PS templates were held vertically, and the Sn(II) solution was slowly dripped on them. The samples were dried at room temperature for 24 h. This infiltration and drying process was repeated for twice. The obtained samples were sintered in air at 450 °C for 1 h using a heating ramp rate of 10 °C min^{-1}, forming ~6 μm-thick SnO_2 scaffolds.

SiO_2 coating and the caged SnO_2 sphere growth. To grow SnO_2 inside the scaffold, a SiO_2 layer was first coated onto the SnO_2 foam using a Stöber method. Typically, 50 mL of Millipore water and 1 mL of ammonium hydroxide (~28%, Sigma-Aldrich Corp.) were mixed with 40 mL of ethanol. A SnO_2 scaffold substrate held by a clamp was immersed into the obtained solution. Then, 0.5 mL of tetraethylorthosilicate (TEOS, Sigma-Aldrich Corp.) was added dropwise into the solution under magnetic stirring at a rate of 400 revolutions per minute (RPM). After 1 h, the substrate was removed, washed with ethanol and water, and dried at 60 ºC for 4 h. The SnO_2 layer inside the scaffold was grown *via* a hydrothermal route similar to literature report[41] with the modifications noted here. Typically, 0.162 g of $K_2SnO_3 \cdot H_2O$ and 1 g of urea were put into 35 mL of Millipore water/ethanol (1:1 vol. ratio) mixture under stirring. Then, the solution was transferred into a 50 mL Teflon-lined steel autoclave. A SiO_2-coated SnO_2 foam on a W substrate was placed into the solution face up. The autoclave was sealed, heated at 180 °C for 12 h and then cooled naturally to room temperature. The sample was removed, washed with ethanol and Millipore water, and dried at 60 °C for 4 h.

SiO_2 removal, carbon coating and reducing treatment. To remove the SiO_2 after hydrothermal growth, a 5% HF in Millipore water/ethanol (1:1 vol. ratio) solution was used to etch the SiO_2. The sample was then washed with Millipore water, and dried at 60 ºC for 6 h. Subsequently, for coating a carbon layer, similar to our previous report,[15] a furfuryl alcohol-based polymerization approach

was employed. Typically, the sphere-caged SnO_2 scaffold substrates were dipped into furfuryl alcohol. The wet sample was then heated in air at 150 ºC for 24 h to polymerize the furfuryl alcohol. At last, the sample was heat treated at 600 ºC for 4 h in a H_2/Ar gas (H_2: 5% vol.), forming a 3D sphere-caged Sn/C composite.

Thick electrode fabrication. Thick electrodes were fabricated started using a 3D mesoporous Ni scaffold following a similar process as for the thin electrodes. See Supporting Information Information (Figure S7) for fabrication details.

Characterization. Samples were characterized using a Hitachi S-4800 SEM, a Philips X'pert MRD XRD with Cu Kα radiation (1.5418 Å), and a JEOL 2100 Cryo TEM operating at 200 kV. The XRD peaks were compared with the Joint Committee on Powder Diffraction Standards. The carbon content in the Sn/C composite was analyzed using a Mettler-Toledo TGA 851e under an air atmosphere and a heating ramp rate of 10 °C min^{-1} from 25 to 500 °C. Raman spectra were obtained on a Nanophoton Raman-11 Laser Raman Microscope system using a laser power of 1.5 mW at 532 nm.

In-situ TEM observations. A nano-battery system in which the Sn/C nanocomposite as anode was prepared for *in-situ* TEM observations. Here, a Li metal flake with a thin Li_2O layer as solid electrolyte was used rather than an ionic liquid due to minimize wetting problems. A small Li_2O-coated Li flake was connected to a W wire as the counter electrode. The Sn/C nanocomposites were then attached on the tip of an Al wire using conductive silver epoxy as the working electrode. The two electrodes were installed on a Nanofactory STM-TEM *in-situ* holder. The *in-situ* study was performed on a JEOL-2010 field emission electron microscope (at 200 kV). The anode was checked by performing potentiostatic discharge at different voltages ranging from 0 to 4 V with respect to the counter electrode. During the discharging, images and movies were taken to monitor the

structure evolution including the morphology, volume and phase changes.

Electrochemical measurements. Electrochemical tests were conducted using two-electrode coin cells using Princeton Applied Research Model 273A and Biologic VMP3 potentiostats. The 3D sphere-caged Sn/C composites were set as the working electrodes. For half cells, lithium metal was used as the counter and reference electrode; while for full cells, a commercial $LiMn_2O_4$ cathode provided by Xerion Advanced Battery was used. All cells were assembled in an Ar-filled glove box. In the full cell, compared to the capacity of anode, the excess capacity of cathode is set at about 10% to reduce the lithium plating during cycling. The Sn/C anode was pre-cycled in a half cell system (*vs.* Li foil) for 15 cycles before the full cell assembly. An electrolyte consisting of 1 M $LiPF_6$ dissolved in a 50:50 (w/w) mixture of ethylene carbonate and diethyl carbonate was used. A polypropylene micro-porous film was employed as the separator. Electrode capacities in half cells were measured by a galvanostatic charge-discharge method at a rate of 0.5C over the potential range of 0.01 to 2 V; while the full cells were cycled at 2C over the voltage range of 2 to 4 V. CV curves were recorded over the potential range of 0 to 2 V (*vs*. Li^+/Li) at a scan rate of 0.1 mV s^{-1}. In C-rate performance measurements, the C-rates were changed from 0.2C to 0.5C, 1C, 5C, 10C, and back to 0.2C. At each of the C-rate, the electrode was cycled 10 times.

ASSOCIATED CONTENT

Supporting Information

SEM images of samples during anode fabrication, Raman, TGA, XRD and electrochemical characterizations of the anodes, thick electrode fabrication procedures, and SEM images of the electrodes after lithiation and delithiation. This material is available free of charge via the Internet at http://pubs.acs.org.

AUTHOR INFORMATION

Corresponding Author

* E-mail: pbraun@illinois.edu.

Notes

The authors declare no competing financial interest.

ACKNOWLEDGMENTS

Sample fabrication and characterization were carried out in the Frederick Seitz Materials Research Laboratory at the University of Illinois at Urbana-Champaign. All authors except Xi Chen, Prof. Junjie Niu, Prof. Xingjiu Huang, and Prof. Jinhuai Liu acknowledge the support from the U.S. Department of Energy, Office of Science, Basic Energy Sciences, under award # DE-FG02-07ER46471. Prof. Xingjiu Huang and Prof. Jinhuai Liu acknowledge support from the State Key Project of Fundamental Research for Nanoscience and Nanotechnology of China (2011CB933700). Prof. Junjie Niu and Xi Chen acknowledge supports from the UW System Applied Research Grant Program (ARG) under award # 106-Y-06-8000-4 and UWM Start-up. We also thank Prof. Ju Li and Dr. Akihiro Kushima at MIT for helps and good suggestions.

REFERENCES

(1) Nitta, N.; Wu, F. X.; Lee, J. T.; Yushin G. *Mater. Today* **2015**, *18*, 252–264.

(2) Goodenough, J. B. *Acc. Chem. Res.* **2013**, *46*, 1053–1061.

(3) Dunn, J. B.; Gaines, L.; Kelly, J. C.; James, C.; Gallagher, K. G. *Energy Environ. Sci.* **2015**, *8*, 158–168.

(4) Wang, C.; Wang, S.; He, Y. B.; Tang, L. K.; Han, C. P.; Yang, C.; Wagemaker, M.; Li, B. H.; Yang, Q. H.; Kim, J. K.; Kang, F. Y. *Chem. Mater.* **2015**, *27*, 5647–5656.

(5) Allcorn, E.; Manthiram, A. *J. Mater. Chem. A* **2015**, *3*, 3891–3900.

(6) Xu, Y. H.; Guo, J. C.; Wang, C. S. *J. Mater. Chem.* **2012**, *22*, 9562–9567.

(7) Son, I. H.; Park, J. H.; Kwon, S.; Park, S.; Rummeli, M. H.; Bachmatiuk, A.; Song, H. J.; Ku, J.; Choi, J. W.; Choi, J. M.; Doo, S. G.; Chang, H. *Nat. Commun.* **2015**, *6*, 7393.

(8) Li, N.; Song, H. W.; Cui, H.; Yang, G. W.; Wang, C. X. *J. Mater. Chem. A* 2014, **2**, 2526−2537.

(9) Fauteux, D.; Koksbang, R. *J. Appl. Electrochem.* **1993**, *23*, 1–10.

(10) Goriparti, S.; Miele, E.; Angelis, F. D.; Fabrizio, E. D.; Zaccaria, R. P.; Capigli, C. *J. Power Sources* **2014**, *257***,** 421−443.

(11) Chen, J. J. *Materials* **2013**, *6*, 156–183.

(12) Ji, L.; Lin, Z.; Alcoutlabi, M.; Zhang, X. *Energy Environ. Sci.* **2011**, *4*, 2682–2689.

(13) Guo, J.; Yang, Z.; Archer, L. A. *J. Mater. Chem. A* **2013**, *1*, 8710–8715.

(14) Liu, J. Y.; Zhang, H. G.; Wang, J. J.; Cho, J.; Pikul, J. H.; Epstein, E. S.; Huang, X. J.; Liu, J. H.; King, W. P.; Braun, P. V. *Adv. Mater.* **2014**, *26*, 7096–7101.

(15) Liu, J. Y.; Li, N.; Goodman, M. D.; Zhang, H. G.; Epstein, E. S.; Huang, B.; Pan, Z.; Kim, J. W.; Choi, J. H.; Huang, X. J.; Liu, J. H.; Hsia, K. J.; Dillon, S. J.; Braun, P. V. *ACS Nano* **2015**, *9*, 1985–1994.

(16) Zhang, H. G.; Yu, X. D.; Braun, P. V. *Nat. Nanotechnol.* **2011**, *6*, 277–281.

(17) Pikul, J. H.; Zhang, H. G.; Cho, J.; Braun, P. V.; King, W. P. *Nat. Commun.* **2013**, *4*, 1732.

(18) Huang, X.; Chen, J.; Lu, Z. Y.; Yu, H.; Yan, Q. Y.; Hng, H. H. *Sci. Rep.* **2013**, *3*, 2317.

(19) Mazouzi, D.; Reyter, D.; Gauthier, M.; Moreau, P.; Guyomard, D.; Roue, L.; Lestriez, B. *Adv. Energy Mater.* **2014**, *4*, 1301718.

(20) Wen, W.; Wu, J. M.; Cao, M. H. *Nano Energy* **2013**, *2*, 1383–1390.

(21) Liu, J.; Kopold, P.; van Aken, P. A.; Maier, J.; Yu, Y. *Angew. Chem. Int. Edit.* **2015**, *54*, 9632–9636.

(22) Liu, N.; Lu, Z.; Zhao, J.; McDowell, M. T.; Lee, H. W.; Zhao, W.; Cui, Y. *Nat. Nanotechnol.* **2014**, 9, 187–192.

(23) Liu, N.; Wu, H.; Mcdowell, M. T.; Yao, Y.; Wang, C.; Cui, Y. *Nano Lett.* **2012**, *12*, 3315–3321.

(24) Ning, H. L.; Mihi, A.; Geddes, J. B.; Miyake, M.; Braun, P. V. *Adv. Mater.* **2012**, *24*, OP153–OP158.

(25) Hassoun, J.; Reale, P.; Panero, S. *J. Power Sources* **2007**, *174*, 321–327.

(26) Elia, G. A.; Panero, S.; Savoini, A.; Scrosati, B.; Hassoun, J. *Electrochim. Acta* **2013**, *90*, 690–694.

(27) Hassoun, J.; Wachtler, M.; Wohlfahrt-Mehrens, M.; Scrosati, B. *J. Power Sources* **2011**, *196*, 349–354.

(28) Wen, C. J.; Huggins, R. A. *J. Electrochem. Soc.* **1981**, *128*, 1181–1187.

(29) Winter, M.; Besenhard, J. O.; Spahr, M. E.; Novak, P. *Adv. Mater.* **1998**, *10*, 725–763.

(30) Yuvaraj, S.; Karthikeyan, K.; Vasylechko, L.; Selvan, R. K. *Electrochim. Acta* **2015**, *158*, 446–456.

(31) Wu, C.; Maier, J.; Yu, Y. *Adv. Funct. Mater.* **2015**, *25*, 3488–3496.

(32) Liao, J. Y.; Manthiram, A. *Adv. Energy Mater.* **2014**, *4*, 1400403.

(33) Wang, B.; Li, X. L.; Qiu, T. F.; Luo, B.; Ning, J.; Li, J.; Zhang, X. F.; Liang, M. H.; Zhi, L. J. *Nano Lett.* **2013**, *13*, 5578–5584.

(34) Kim, J.; Oh, C.; Chae, C.; Yeom, D. H.; Choi, J.; Kim, N.; Oh, E. S.; Lee, J. K. *J. Mater. Chem. A* **2015**, *3*, 18684–18695.

(35) Chen, J. J.; Yano, K. *ACS Appl. Mater. Interfaces* **2013**, *5*, 7682–7687.

(36) Freire, M.; Kosova, N. V.; Jordy, C.; Chateigner, D.; Lebedev, O. I.; Maignan, A.; Pralong, V. *Nat. Mater.* **2016**, *15*, 173–179.

(37) Put, B.; M. Vereecken, P. M.; Labyedh, N.; Sepulveda, A.; Huyghebaert, C.; Rad, I. P.; Stesmans, A. *ACS Appl. Mater. Interfaces* **2015**, *7*, 22413–22420.

(38) Kim, D. K.; Muralidharan, P.; Lee, H. W.; Ruffo, R.; Yang, Y.; K. Chan, C. K.; Peng, H. L.; Huggins, R. A.; Cui, Y. *Nano Lett.* **2008**, *8*, 3948−3952.

(39) Cheng, F. Y.; Wang, H. B.; Zhu, Z. Q.; Wang, Y.; Zhang, T. R.; Tao, Z. L.; Chen, J. J. *Energy Environ. Sci.* **2011**, *4*, 3668−3675.

(40) Niu, J. J.; Kushima, A.; Qian, X. F.; Qi, L.; Xiang, K.; Chiang, Y. M.; Li, J. *Nano Lett.* **2014**, *14*, 4005–4010.

(41) Kim, W. S.; Hwa, Y.; Jeun, J. H.; Sohn, H. J.; Hong, S. H. *J. Power Sources* **2013**, *225*, 108–112.

TOC Graphic: